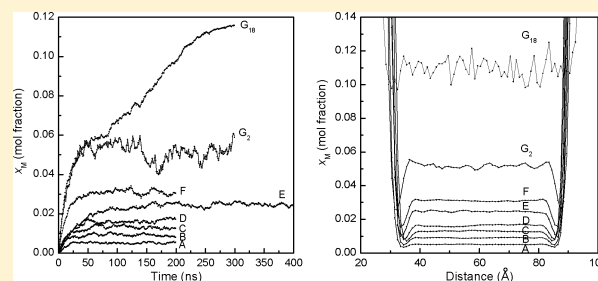


# Solubility of Aqueous Methane under Metastable Conditions: Implications for Gas Hydrate Nucleation

Guang-Jun Guo<sup>\*,†,‡</sup> and P. Mark Rodger<sup>‡</sup><sup>†</sup>Key Laboratory of the Earth's Deep Interior, Institute of Geology and Geophysics, Chinese Academy of Sciences, Beijing 100029, People's Republic of China<sup>‡</sup>Centre for Scientific Computing and Department of Chemistry, University of Warwick, Coventry CV4 7AL, United Kingdom**S** Supporting Information

**ABSTRACT:** To understand the prenucleation stage of methane hydrate formation, we measured methane solubility under metastable conditions using molecular dynamics simulations. Three factors that influence solubility are considered: temperature, pressure, and the strength of the modeled van der Waals attraction between methane and water. Moreover, the naturally formed water cages and methane clusters in the methane solutions are analyzed. We find that both lowering the temperature and increasing the pressure increase methane solubility, but lowering the temperature is more effective than increasing the pressure in promoting hydrate nucleation because the former induces more water cages to form while the latter makes them less prevalent. With an increase in methane solubility, the chance of forming large methane clusters increases, with the distribution of cluster sizes being exponential. The critical solubility, beyond which the metastable solutions spontaneously form hydrate, is estimated to be  $\sim 0.05$  mole fraction in this work, corresponding to the concentration of 1.7 methane molecules/nm<sup>3</sup>. This value agrees well with the cage adsorption hypothesis of hydrate nucleation.

**■ INTRODUCTION**

A metastable liquid exists under conditions where the thermodynamic phase diagram indicates the substance has a more stable phase, and it is of great significance in nature and technology.<sup>1</sup> Alongside some well-known examples, such as supercooled and superheated water, the aqueous solutions of hydrophobic gases at high pressures and low temperatures are an important example, with the liquid being metastable with respect to gas hydrates. In this paper, we focus on methane hydrate because it is a potential energy resource in the world.<sup>2</sup> When a methane solution is brought into the phase region of methane hydrate stability, one often finds that the hydrate does not crystallize immediately; instead, an induction time is required, usually from several hours to several days. Interestingly, the induction time is shortened if the methane solution was prepared by melting methane hydrate. This phenomenon is the so-called memory effect of hydrates and is still an open topic in hydrate research.<sup>2–6</sup> The most common speculation is that the memory effect is due to excess dissolved gas molecules<sup>3,4</sup> or the residual structure<sup>5</sup> left in the melted hydrates. Obviously, a complete understanding of this phenomenon will ultimately require a knowledge of the hydrate formation mechanism on a molecular level, and how this relates to the thermodynamic driving force for hydrate formation.

Recently, some important progress has been made in elucidating the mechanism of formation of hydrates. The ability to simulate spontaneous hydrate nucleation<sup>7–12</sup> has led to the identification of an amorphous hydrate phase,<sup>10–13</sup> the

proposal of the cage adsorption hypothesis,<sup>14</sup> and two-step mechanisms of hydrate nucleation<sup>10–12</sup> and prompted detailed studies of the structural transformation of hydrate cages.<sup>15,16</sup> A consensus is now emerging that initially an amorphous hydrate phase is nucleated, and that this subsequently transforms to a crystalline hydrate. This Ostwald step rule mechanism continues to be supported by the most recent computer simulation studies.<sup>17–19</sup> However, despite this progress, there is still very little understanding of the structural fluctuations that occur within the metastable methane/water mixture. Because it is these fluctuations that drive nucleation events, characterizing the metastable methane solution remains a key step toward a complete understanding of hydrate nucleation and the memory effect. Because an important feature of the metastable methane solution is methane oversaturation, studying methane solubility is an essential part of this process. However, compared with the wealth of experimental data on methane solubility in thermodynamic equilibrium states, corresponding measurements for metastable states are rare. In particular, the limit of methane supersaturation prior to hydrate formation is unknown.

To shed new light on metastable methane solutions, in this paper, we have examined methane solubility under metastable conditions using molecular dynamics (MD) simulations.

Received: November 28, 2012

Revised: May 1, 2013

Published: May 2, 2013

Table 1. Details of Simulation Systems<sup>a</sup>

system	$N_M$	$N_W$	$T$ (K)	$P$ (bar)	$L_{x(y)}$ (Å)	$\chi$	no. of runs	duration of each run (ns)
A	380	1800	258.5	1.2	29.78	1.07	20	200
B	640	1800	258.5	329.5	29.99	1.07	20	200
C	800	1800	258.5	929.2	30.04	1.07	20	200
D	800	1800	250.0	929.4	29.92	1.07	20	200
E	800	1800	240.0	929.7	29.77	1.07	20	400
F	800	1800	258.5	926.3	29.94	1.20	20	200
G <sub>2</sub>	800	1800	258.5	924.5	29.82	1.30	2	300
G <sub>18</sub>	800	1800	258.5	945.0	29.37	1.30	18	300

<sup>a</sup> $N_M$  and  $N_W$  are the numbers of methane and water molecules, respectively.  $L_{x(y)}$  is the length of the simulation box in the  $x$ - and  $y$ -directions.  $T$ ,  $P$ , and  $\chi$  are the temperature, the pressure, and the factor adjusting the strength of the methane–water attraction, respectively. All systems are inside the hydrate phase region except system A. In addition, system G is classified with two subtypes: G<sub>2</sub>, in which no hydrate formation occurs, and G<sub>18</sub>, in which hydrate formation does occur (see details in the text).

Various factors that can affect the methane solubility have been evaluated, and a detailed analysis of the structure of the resulting metastable phases is presented, including the distribution of methane clusters in water and the occurrence of cagelike water clusters, key order parameters for understanding the development of critical nuclei for hydrate formation.

## METHODS

Using GROMACS,<sup>20</sup> the initial configuration for a water film was created by combining equilibrated configurations from two bulk gaseous methane simulations (dimensions of 30 Å × 30 Å × 27 Å) and one bulk liquid water simulation (30 Å × 30 Å × 57 Å) with a methane–water–methane stacking pattern, leaving a gap of 3 Å at each interface to give a combined cuboid box of 30 Å × 30 Å × 120 Å. The Nosé–Hoover thermostat and Parrinello–Rahman barostat, with a period of 1.0 ps for both, were used to obtain the  $NPT$  ensemble. The Parrinello–Rahman pressure coupling was semi-isotropic, allowing the simulation box size to vary in the  $x$ - and  $y$ -directions but keeping it fixed in the  $z$ -direction. Periodic boundary conditions were used in all directions. To maintain comparable water film dimensions in all simulations, the number of water molecules in the system was fixed at 1800, and the total number of methane molecules was chosen to give an average  $x$ – $y$  cross section for the simulation box of 30 Å × 30 Å; the number of methane molecules therefore varied between 380 and 800, depending on the pressure.

The TIP4P/2005 potential<sup>21</sup> was used to describe water interactions and the OPLS-UA potential<sup>22</sup> for methane. Modified Lorentz–Berthelot combining rules were adopted for the cross interaction between water and methane, which means

$$\sigma_{MO} = (\sigma_M + \sigma_O)/2$$

$$\epsilon_{MO} = \chi \sqrt{\epsilon_M \epsilon_O}$$

where  $\sigma$  and  $\epsilon$  are parameters in the Lennard–Jones potential function that is often used to describe the van der Waals force and subscripts M and O represent methane and water oxygen, respectively. In addition,  $\chi$  is a factor used to adjust the strength of cross interaction between methane and water, with a  $\chi$  value of 1 giving the standard Lorentz–Berthelot combining rules.  $\chi$  determines the nonideality of guest–water mixing, with larger values representing more hydrophilic guests. According to the work of Docherty et al.,<sup>23</sup> a  $\chi$  value of 1.07 gives an excellent representation of the excess chemical potential for methane in

water at infinite dilution for temperatures in the range of 280–370 K, and of the unit cell dimensions for methane hydrate from 180 to 270 K. The model also predicts methane/water/hydrate three-phase equilibrium temperatures to within 5% for pressures in the range of 40–400 bar.<sup>24</sup> We note, finally, that this water potential was developed to reproduce the density of liquid water from 245 to 380 K and conclude that this is an excellent set of potentials with which to model methane/water mixtures that are metastable with respect to methane hydrate. Some simulations were also performed with  $\chi$  values of 1.20 and 1.30 to assess the sensitivity of the structure of the solution to the guest/water attractive forces.

In this work, we simulated seven separate systems, A–G (Table 1), adjusting three factors ( $T$ ,  $P$ , and  $\chi$ ) that affect the methane solubility. In each case, 20 distinct simulations were performed to provide an accurate result. Among the seven systems, A–C had uniform conditions for everything except  $P$ , which was varied from 1.2 to 929.2 bar; only  $T$  varied for systems C–E, from 258.5 to 240 K, and systems C, F, and G differ only in the choice of  $\chi$ , which was varied from 1.07 to 1.30. Additionally, all these systems (except system A) are inside the hydrate region of the phase diagram. System G is classified with two subtypes: G<sub>2</sub>, in which no hydrate formation occurs during the simulations, and G<sub>18</sub>, in which hydrate formation does occur (see details in Results). Overall, the A–G labeling indicates the order of increasing methane solubility.

When these simulations were performed, two interfaces between methane and water formed very quickly, and then methane molecules gradually began to dissolve into the liquid water. To monitor the solubility profile of the system, we divided the  $z$ -dimension (i.e., the dimension perpendicular to the interfaces) into 120 parallel slabs with thicknesses of 1 Å and counted the number of methane and water molecules in each slab; these data were used to calculate the mass density profile,  $\rho$ , and the methane solubility profile,  $x_M(z)$  in mole fraction, across the interfaces. Typical profiles for  $x_M(z)$  and  $\rho$  are shown in Figure 1: from gas to solution phase, the mole fraction of methane shows a sharp, monotonic decrease over a distance of  $\sim 15$  Å; there is a corresponding sharp increase in density, but in this case, it is not monotonic, with a maximum occurring on the water side of each interface. The separate density profiles for water and methane are shown in Figure 2: the methane density shows a peak ( $z = 26$  or  $94$  Å) on the gas side and a valley ( $z = 35$  or  $85$  Å, more pronounced under other conditions, as seen in Figure S1 of the Supporting Information) on the water side of each interface, while the water density shows a peak ( $z = 34$  or  $86$  Å) only on the water

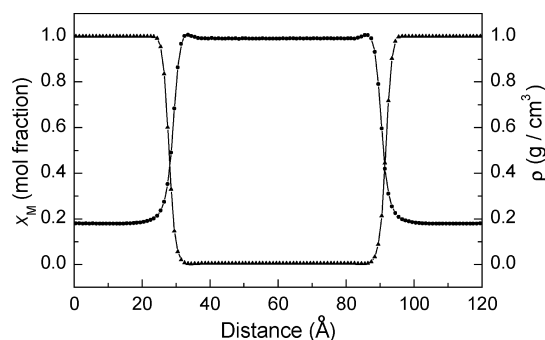


**Figure 1.** Typical profiles across the interfaces of the system, taking system A as an example and calculated from the last 100 ns of the trajectories. Triangles denote the methane solubility ( $x_M$ ) and circles the system density ( $\rho$ ).

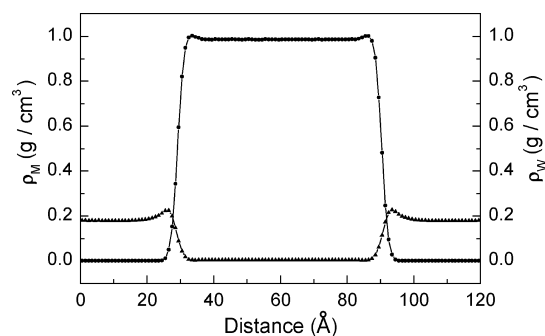


**Figure 2.** Density profiles of system A for methane ( $\blacktriangle$ ) and water ( $\bullet$ ) separately.

side. The  $x_M(z)$  profiles for all systems are presented below, and the density profiles for all systems can be found in Figures S1 and S2 of the Supporting Information. For the purposes of this paper, we have taken the middle 30 Å of the water film (i.e., the range of 45–75 Å) to represent the bulk liquid, but note that we have not performed simulations to analyze the effect of film thickness.

We further analyzed the water films to characterize the occurrence of water cages and the methane clusters. In this paper, we use “cages” to refer to face-saturated cages, as defined in our previous work,<sup>13,25</sup> and include both complete and incomplete cages. Two methane molecules were defined to be connected when the distance between them was <5.3 Å (the first minimum in the methane–methane radial distribution function). Methane molecules were then defined as belonging to the same cluster if they were linked by an unbroken network of connected methane pairs.

## RESULTS

The time evolution of  $x_M(t)$  (mean value between 45 and 75 Å) is shown in Figure 3. For most of the systems, dissolution of methane reaches a steady state within 100 ns. The process is slower in system E, the lowest temperature considered, where 200 ns is needed to establish the steady state solubility of methane. Additionally, when averaged over all 20 simulations, system G does not show a plateau. Closer inspection of system G showed that the continuing dissolution of methane was actually caused by the nucleation and growth of hydrate in 18 of the 20 separate simulations: this was in the form of the amorphous hydrate observed in other simulations,<sup>13</sup> viz., a space-filling solid composed of various water cages but

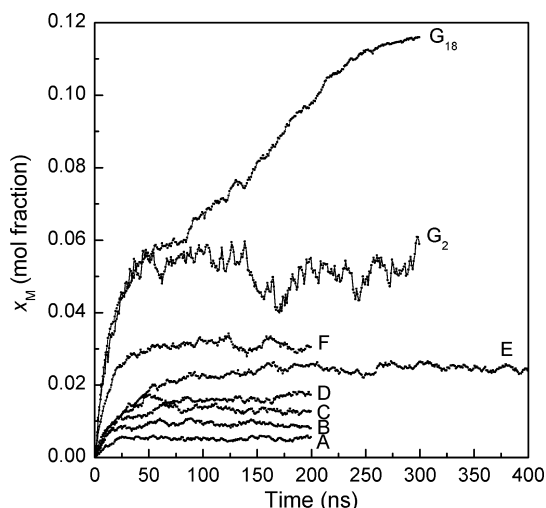


**Figure 3.** Time evolution of  $x_M(t)$  for all systems. The data were calculated from the middle of the water film (45–75 Å) in each simulation box. Each point represents a block average over 1 ns.

assembled without long-range spatial order and partially filled with methane. The other two simulations showed behavior analogous to that of systems A–F (see Figures S3 and S4 of the Supporting Information). We therefore selected the two simulations that did not show hydrate formation, denoted collectively as  $G_2$ , to represent the metastable liquid film and used the remaining 18 simulations (denoted  $G_{18}$ ) to represent a hydrate-forming system. In the following, we uniformly took the last 100 ns of each simulation as the sample for analyzing the (metastable) equilibrium.

Figure 4 shows the solubility profiles of methane,  $x_M(z)$  (averaged over the last 100 ns of simulation), for all systems. All

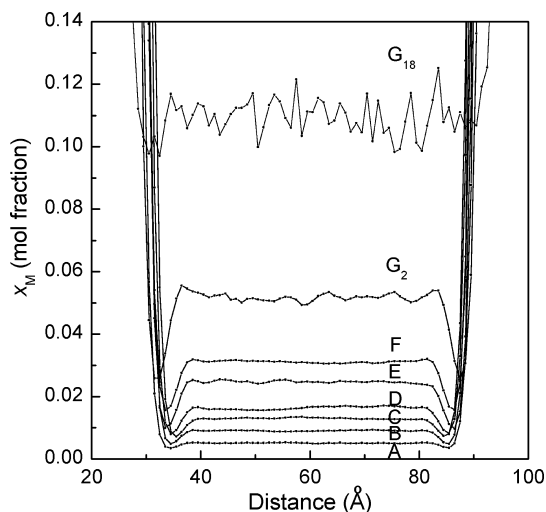


**Figure 4.** Profiles of  $x_M(z)$  for all systems. The data are calculated from the last 100 ns of each simulation, and each point represents the average over a 1 Å thick slab.

systems are consistent with a homogeneous distribution of methane across the water film (ca. 40–80 Å), albeit with substantial noise for the hydrate-forming system ( $G_{18}$ ). On the basis of Figures 3 and 4, we conclude that systems A– $G_2$  reach an apparent equilibrium state with respect to both space and time. For system A, this is the thermodynamic equilibrium, as

**Table 2. Structural Characterization of Methane Solutions under the Equilibrium (system A) and Metastable (systems B–G<sub>2</sub>) Conditions<sup>a</sup>**

system	$N_M$	$N_W$	$x_M$	$C_M$ (nm <sup>-3</sup> )	$C_{\text{cage}}$ (nm <sup>-3</sup> )	$\rho$ (g/cm <sup>3</sup> )	$f_{M\text{-ad}}$
A	4.5(2)	877(1)	0.0051(2)	0.17(1)	0.246(0)	0.9901(2)	0.214(0)
B	8.2(3)	899(1)	0.0091(4)	0.30(1)	0.227(1)	1.0046(4)	0.201(0)
C	12.2(3)	920(1)	0.0131(3)	0.45(1)	0.200(1)	1.0284(3)	0.179(0)
D	15.1(3)	905(1)	0.0164(3)	0.56(1)	0.255(1)	1.0238(4)	0.226(1)
E	22.3(7)	880(2)	0.0247(8)	0.84(3)	0.365(3)	1.0119(9)	0.309(2)
F	28.2(4)	882(1)	0.0310(5)	1.05(1)	0.240(1)	1.0089(5)	0.209(1)
G <sub>2</sub>	45.7(15)	842(3)	0.0514(17)	1.71(5)	0.288(3)	0.9902(15)	0.248(1)

<sup>a</sup>These parameters are calculated from the sampling area (i.e.,  $45 \text{ \AA} \leq z \leq 75 \text{ \AA}$ ) for the last 100 ns.  $N_M$  and  $N_W$  are the numbers of methane and water molecules, respectively. The methane solubility is defined as  $x_M = N_M/(N_M + N_W)$  and the corresponding concentration  $C_M = N_M/V$ , where  $V$  is the volume of the sampling area. The cage concentration  $C_{\text{cage}} = N_{\text{cage}}/V$ , where  $N_{\text{cage}}$  is the number of cages.  $\rho$  is the total mass density of methane solutions, and  $f_{M\text{-ad}}$  is the fraction of the dissolved methane molecules that are adsorbed on cages. The water cages and adsorbed methane are identified using the FSICA method.<sup>13</sup> The numbers in parentheses are the standard errors, calculated from the 20 independent runs for systems A–F and two independent runs for system G<sub>2</sub>.

the state is outside the hydrate region of the phase diagram. For systems B–G<sub>2</sub>, this is more likely to represent a metastable state. The calculated “bulk” values of  $x_M$  are listed in Table 2.

Additionally, we identified all methane clusters formed in the systems and calculated the probability distribution of finding a methane in a given size cluster (Figure 5); we stress that this

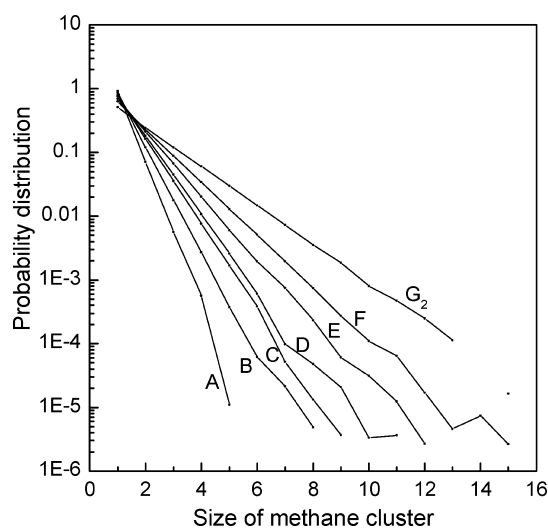


**Figure 5.** Probability distribution of finding a methane in a given size cluster.

analysis was for methane molecules found within the central region of the water film (i.e.,  $45 \text{ \AA} \leq z \leq 75 \text{ \AA}$ ) and relates to methane–methane contact, not solvent-separated methane as would be found in hydrate clusters. Not surprisingly, with increasing methane solubility from system A to G<sub>2</sub> (Table 2), methane molecules are found in clusters with greater and greater frequency. While the percentage of dissolved methane found as single (dissolved) molecules decreases (see the cluster size of 1 in Figure 5), from 92% in system A to 52% in system G<sub>2</sub>, the concentration of single (dissolved) methane molecules still increases 5-fold across this series, contributing 0.0047 to the  $x_M$  in system A up to 0.0266 for system G<sub>2</sub>. Intriguingly, the concentration of cages does not mimic the variation in methane solubility. This point will be considered further in the discussion, although further comment on the types of cages observed is useful at this point: most were observed to be small, empty, face-saturated incomplete cages, similar to the previous

results for methane solutions prior to hydrate nucleation (see Table 6 and Table S3 of ref 13).

A very clear feature in Figure 5 is the linearity of the distribution functions on the semilog plot, indicating that the cluster size distribution is, in all cases, exponential. For equilibrium systems, the probability distribution is given by  $\exp(-G_n/kT)$ , where  $G_n$  is the Gibbs free energy of the system with a cluster of  $n$  methane molecules. Thus, Figure 5 also indicates that the reduced Gibbs free energy,  $G_n/kT$ , increases linearly with  $n$ . This is inconsistent with classical nucleation theory,<sup>26</sup> which describes  $G_n$  as the sum of a positive surface energy (varies as  $n^{2/3}$ ) and a negative bulk energy (varies as  $n^1$ ), and so indicates that these clusters are not potential nuclei for methane bubble formation. The slopes of the free energy curve with respect to cluster size give the free energy for attaching a methane molecule to an existing cluster, and values obtained from Figure 5 are listed in Table 3; we note that this

**Table 3. Free Energies for Methane Cluster Formation<sup>a</sup>**

system	$\Delta G_1/kT$	system	$\Delta G_1/kT$
A	2.55	E	1.11
B	1.91	F	0.91
C	1.56	G <sub>2</sub>	0.70
D	1.42		

<sup>a</sup> $\Delta G_1$  is the free energy needed to add one methane molecule to an existing cluster and is obtained as the slope of the semilog plots in Figure 5.

attachment energy is significantly less than the thermal energy ( $kT$ ) only for system G<sub>2</sub>. The free energy differences do indicate that the clusters will readily dissolve once hydrate formation begins to deplete the concentration of single dissolved methane molecules, so that the clusters provide a ready source of methane within the water phase to support rapid initial hydrate growth once nucleation does occur.

## DISCUSSION

We first focus on system A, performed at 258.5 K and 1.2 bar. Considering that the melting point of TIP4P/2005 water is 250 K and in comparison to the phase diagram of methane hydrate based on this water model,<sup>24</sup> the thermodynamically stable state for system A is the liquid film. Thus, in the context of methane hydrate formation, this system provides a good representation of an equilibrium methane solution. However, the calculated  $x_M$

for system A is 0.005 mole fraction in this study, which is much larger than the experimental values of  $x_M$  under an equivalent condition, for example, 0.00004 mole fraction at 280 K.<sup>27</sup> The potentials used in this work are known to reproduce the experimental density of water<sup>21</sup> and the methane excess chemical potential for infinitely dilute aqueous solution;<sup>23</sup> they also reproduce a number of properties of methane hydrate<sup>23,24</sup> across a range of temperatures and pressures that includes the thermodynamic state of system A. We therefore think it unlikely that this discrepancy is an artifact of the potentials used. Instead, we suggest that it may be a real consequence of small system size. Recent X-ray reflectivity experiments have identified an enhanced concentration of Xe within the first 3–5 nm of water at a gas–water interface, which was interpreted as a supersaturation of Xe in this 3–5 nm zone.<sup>28</sup> Methane and Xe are well-known exemplars of the law of corresponding states, and both form type I hydrates. It is therefore not unreasonable to suggest that methane could also show a supersaturation within a nanometer-scale interfacial zone, in which case the methane concentration would not converge to the bulk value within the 7 nm water film used in the study presented here. Additionally, by using in situ neutron reflectivity, Koga et al.<sup>29</sup> found that the surface of water becomes rougher when the water phase contacts methane gas and speculated that this is due to the formation of microscopic hydrate embryos in a dynamic equilibrium manner. This would again be consistent with a high concentration of methane on the water side of the gas–liquid interface. As for the aspect of computer simulation, our results do agree with recent MD simulations,<sup>30</sup> which reported values of  $x_M$  of  $>0.015$  before hydrate nucleation. However, enhanced methane solubility was not observed in simulations<sup>31</sup> in which the water film was formed as a bridge between two hydroxylated silica surfaces, although the authors did report a very strong influence of the silica on the behavior of the water within the film. We think their simulation time is too short [only 2 ns, and at least 50 ns was needed (see Figure 3)] to reach a steady state of dissolving methane into water and thus results in the low methane solubility in the water film. Further work is needed to characterize the length scale of the effect of any thin film on gas solubility in hydrate-forming systems, but that is beyond the scope of this work.

Trends in the concentration of water cages are particularly important in the context of hydrate nucleation. The data in Table 2 show that cage formation is more strongly affected by thermodynamic state than it is by methane concentration:  $C_M$  increases with increasing  $P$ , with decreasing  $T$ , and with increasing  $\chi$  (Figure 6). When just one of these three factors is varied, a linear relationship between methane concentration and cage formation is recovered, but the gradient associated with this linear relationship changes considerably depending on whether the underlying variable is  $T$ ,  $P$ , or  $\chi$ . Most importantly, the gradient is positive for  $T$  and  $\chi$  but negative for  $P$ . Because the occurrence of cages is another critical factor for hydrate formation, decreasing  $T$  is a more effective means of triggering hydrate nucleation than is increasing  $P$ . In other words, if the system pressure is increased isothermally, more methane molecules dissolve into water but the number of water cages is reduced. The reduction in cage number occurs because most cages are empty and so tend to collapse under pressure. These two changes in solution are contradictory for hydrate formation. On the other hand, when the temperature is decreased isobarically, the concentration of both methane and

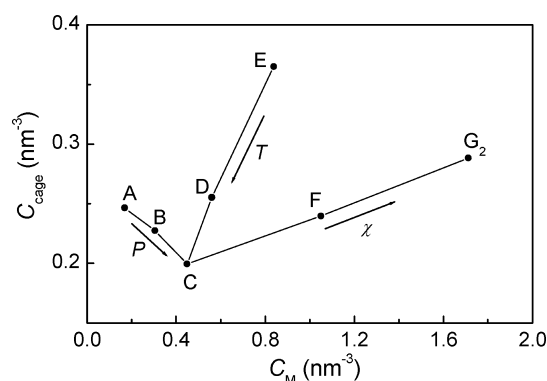


**Figure 6.** Relationship between methane concentration and cage concentration in solutions. The arrows point in the increasing direction of the corresponding parameters.

water cages will increase, both of which should promote hydrate formation. These different effects of increasing pressure and decreasing temperature are also seen in the methane–methane radial distribution functions {RDFs [see  $g(r)_{MM}$  in Figures S5 and S6 of the Supporting Information]}. A decreasing temperature causes the height of the first peak to decrease and the second to increase and shift to smaller  $r$ ; all of these changes shift the RDF toward that observed in the hydrate-forming system,  $G_{18}$ . In contrast, increases in pressure cause the heights of both peaks to increase, essentially being contradictory to do so.

Because a given guest species corresponds to a constant  $\chi$  value, variations in  $\chi$  are equivalent to changing the guest species in experiments. This computational alchemy provides great control of how the interactions are changed and so can provide considerable insight into the nature of the interactions that drive hydrate formation. Increasing  $\chi$  is equivalent to choosing a less hydrophobic guest molecule and hence increasing the guest solubility in water but does so in a way that does not change the corresponding gas phase equation of the state; it thus allows us to distinguish unambiguously between the influence of guest solubility and  $T$ - and  $P$ -related changes on water structure in hydrate nucleation.

Given this perspective, it is interesting to note that hydrate nucleation was observed in only one of our systems, G (including  $G_2$  and  $G_{18}$ ), and that for this system it was observed in 18 of 20 simulations. As can be seen in Figure 6, the variations in  $\chi$  considered in this work lead to a greater variation in guest concentration than did the variations in temperature but had far less influence on water cage formation: lowering the temperature produces more cages, whereas increasing  $\chi$  produces more solute molecules. The methane–methane RDFs are quite consistent with the observation described above. In Figures S6 and S7 of the Supporting Information, both lowering  $T$  and increasing  $\chi$  reduce the height of the first peak and increase that of the second peak. It is the latter that has proven to be effective in producing hydrate nucleation and so suggests that there is a critical solubility above which hydrate nucleation becomes nearly instantaneous. Because 90% of the simulations for system G began to form hydrate within 300 ns, this critical solubility can be estimated from the two remaining metastable states to be  $\sim 0.05$  mole fraction:  $1/3$  of the methane solubility in hydrate and 10 times the equilibrium solubility of system A.

The concept of critical solubility, beyond which the metastable solutions cannot persist, can be explained by the

cage adsorption hypothesis (CAH) of hydrate nucleation.<sup>14</sup> The CAH emphasizes that the adsorption interaction between a cage and methane is the intrinsic driving force for hydrate formation. When a methane molecule approaches a cage, there is an energy barrier located  $\sim 8.8$  Å from the cage that must be crossed before the methane molecule can adsorb to the outside of a cage face. This barrier therefore inhibits methane molecules from aggregating to induce hydrate nucleation and thus allows the methane solution to be metastable with respect to hydrate formation. In system G<sub>2</sub>, the mole fraction of dissolved methane is 0.05, corresponding to the concentration of 1.7 methane molecules/nm<sup>3</sup>. This corresponds to an average separation between methane molecules of 8.4 Å, i.e., inside the aforementioned energy barrier to adsorption on a cage face, thus making nucleation extremely probable. There are two other studies in the literature that also induce rapid hydrate nucleation using a high methane concentration. Both give average methane–methane separations that are inside this free energy barrier: 0.08 mole fraction ( $\sim 7.6$  Å methane separation) at the methane–water interface<sup>7,8</sup> and 0.07 mole fraction ( $\sim 8.0$  Å methane separation) in the absence of the interface.<sup>18</sup> In comparison, the average separation between methane molecules in systems A–F, obtained using the  $C_M$  data in Table 2, changes from 18.1 to 9.8 Å; all of these are outside the free energy barrier at 8.8 Å. This shows that forming hydrate in these systems is an activated process and so will involve a much longer nucleation time. Indeed, it is possible that local fluctuations in concentration provide a nucleation mechanism: hydrate nucleation will be triggered in systems B–F over very long times if the methane solubility in some local region of these systems reaches the critical value of  $\sim 0.05$  mole fraction (i.e.,  $C_M = 1.7$  molecules/nm<sup>3</sup>).

Considering the important role of gas solubility in hydrate nucleation, elaborate experiments are needed to measure the gas solubility of metastable aqueous solutions, with a resolution that allows a focus on different regions of solutions, such as the bulk liquid, the water side of the gas–water interface, the surroundings of the hydrate crystal in the liquid, and the vicinity of the container–water interface. In fact, the Raman spectrum has been used to measure methane<sup>32</sup> and hydrogen gas<sup>33</sup> solubility under equilibrium states, and it will provide useful information about hydrate nucleation and growth if one uses it to take similar measures for the metastable gas solutions.

At present, many methods have been suggested for inducing spontaneous hydrate formation in simulations. These include exploiting the high concentration of methane by melting a hydrate crystal,<sup>7,8,18</sup> performing very long MD simulations on the scale of microseconds,<sup>9</sup> adopting a coarse-grained model of water to accelerate calculation,<sup>10,11</sup> imposing thermodynamic gradients during simulations,<sup>12,19</sup> and using silica as the heterogeneous contacting boundary.<sup>17</sup> Compared with these methods, increasing the guest–water interaction parameter,  $\chi$ , is a simple way to realize hydrate nucleation, repeatably, in simulations. This is the simulator's analogue of using help gases in experiments. Although it is somewhat unphysical, the method can be used to obtain spontaneous nucleation trajectories conveniently, and it could also be used to screen particular solutes for experiments and simulations of hydrate formation.

## CONCLUSIONS

To understand the prenucleation stage of methane hydrate formation, we have used MD simulations to measure the

solubility of methane in a thin water film under metastable conditions. The effect of temperature and pressure on gas phase solubility in equilibrium systems has long been known and is reproduced in our simulations of metastable methane solutions: lowering the temperature or increasing the pressure increases the solubility, as is required for forming hydrates. The significance of the simulations is that they allow a detailed analysis of the water structure with a resolution that is not available via experiments. Our analysis shows that lowering the temperature increases the level of cage formation within the water, but increasing the pressure actually suppresses cage formation. Thus, whereas lowering the temperature induces changes in guest solubility and water structure that are both favorable to hydrate formation, for increasing pressure the effects on solubility and water structure tend to cancel. Hence, lowering the temperature is more effective in promoting hydrate nucleation than is increasing the pressure. Direct methane aggregation (i.e., subcritical clusters for bubble formation) was found to vary smoothly with methane solubility, showing an exponential distribution of cluster size. Most of the single methane and small methane cluster diffuse freely in water, but 18–31% of methane molecules are adsorbed to water cages (see the last column in Table 2).

This paper also presents results of simulations with slightly different guest molecules, chosen to vary the hydrophobicity of the guest without changing the gas phase diagram. These simulations have allowed us to separate the influences of water structure and guest solubility in hydrate nucleation to show that there is a critical guest concentration above which hydrate nucleation becomes effectively instantaneous. The critical solubility is found to be  $\sim 0.05$  mole fraction, corresponding to the concentration of 1.7 methane molecules/nm<sup>3</sup>. These results are shown to be in excellent agreement with the cage adsorption hypothesis for hydrate nucleation. In the future, we will study the effect of film thickness on methane solubility and the kinetics of methane dissolving into and escaping from liquid water, which may provide direct evidence to explain the memory effect of hydrates.

## ASSOCIATED CONTENT

### Supporting Information

Profiles of methane density and water density for all systems (Figures S1 and S2), evidence of hydrate formation in system G (Figures S3 and S4), and results of RDF between methane molecules (Figures S5–S7). This material is available free of charge via the Internet at <http://pubs.acs.org>.

## AUTHOR INFORMATION

### Corresponding Author

\*E-mail: [guogj@mail.igcas.ac.cn](mailto:guogj@mail.igcas.ac.cn).

### Notes

The authors declare no competing financial interest.

## ACKNOWLEDGMENTS

This work was supported by the National Basic Research Program of China (i.e., Program 973) via Grant 2009CB219503 and the Chinese Academy of Sciences via Grant KZCX2-EW-118.

## REFERENCES

- (1) Debenedetti, P. G. *Metastable Liquids: Concepts and Principles*; Princeton University Press: Princeton, NJ, 1996.

- (2) Sloan, E. D.; Koh, C. A. *Clathrate Hydrates of Natural Gases*, 3rd ed.; CRC Press: Boca Raton, FL, 2008.
- (3) Rodger, P. M. *Ann. N.Y. Acad. Sci.* **2000**, *912*, 474.
- (4) Buchanan, P.; Soper, A. K.; Thompson, H.; Westacott, R. E.; Creek, J. L.; Hobson, G.; Koh, C. A. *J. Chem. Phys.* **2005**, *123*, 164507.
- (5) Gao, S.; House, W.; Chapman, W. G. *J. Phys. Chem. B* **2005**, *109*, 19090.
- (6) Wilson, P. W.; Haymet, A. D. *J. Chem. Eng. J.* **2010**, *161*, 146.
- (7) Moon, C.; Taylor, P. C.; Rodger, P. M. *J. Am. Chem. Soc.* **2003**, *125*, 4706.
- (8) Hawtin, R. W.; Quigley, D.; Rodger, P. M. *Phys. Chem. Chem. Phys.* **2008**, *10*, 4853.
- (9) Walsh, M. R.; Koh, C. A.; Sloan, E. D.; Sum, A. K.; Wu, D. T. *Science* **2009**, *326*, 1095.
- (10) Jacobson, L. C.; Hujo, W.; Molinero, V. *J. Am. Chem. Soc.* **2010**, *132*, 11806.
- (11) Jacobson, L. C.; Hujo, W.; Molinero, V. *J. Phys. Chem. B* **2010**, *114*, 13796.
- (12) Vatamanu, J.; Kusalik, P. G. *Phys. Chem. Chem. Phys.* **2010**, *12*, 15065.
- (13) Guo, G.-J.; Zhang, Y.-G.; Liu, C.-J.; Li, K.-H. *Phys. Chem. Chem. Phys.* **2011**, *13*, 12048.
- (14) Guo, G.-J.; Li, M.; Zhang, Y.-G.; Wu, C.-H. *Phys. Chem. Chem. Phys.* **2009**, *11*, 10427.
- (15) Walsh, M. R.; Rainey, J. D.; Lafond, P. G.; Park, D.-H.; Beckham, G. T.; Jones, M. D.; Lee, K.-H.; Koh, C. A.; Sloan, E. D.; Wu, D. T.; Sum, A. K. *Phys. Chem. Chem. Phys.* **2011**, *13*, 19951.
- (16) Tang, L.; Su, Y.; Liu, Y.; Zhao, J.; Qiu, R. *J. Chem. Phys.* **2012**, *136*, 224508.
- (17) Bai, D.; Chen, G.; Zhang, X.; Wang, W. *Langmuir* **2012**, *28*, 7730.
- (18) Sarupria, S.; Debenedetti, P. G. *J. Phys. Chem. Lett.* **2012**, *3*, 2942.
- (19) Liang, S.; Kusalik, P. G. *J. Phys. Chem. B* **2013**, *117*, 1403.
- (20) van der Spoel, D.; Lindahl, E.; Hess, B.; van Buuren, A. R.; Apol, E.; Meulenhoff, P. J.; Tieleman, D. P.; Sijbers, A. L. T. M.; Feenstra, K. A.; van Drunen, R.; Berendsen, H. J. C. *Gromacs User Manual version 4.5.3*, 2010; <http://www.gromacs.org>.
- (21) Abascal, J. L. F.; Vega, C. *J. Chem. Phys.* **2005**, *123*, 234505.
- (22) Jorgensen, W. L.; Madura, J. D.; Swenson, C. J. *J. Am. Chem. Soc.* **1984**, *106*, 6638.
- (23) Docherty, H.; Galindo, A.; Vega, C.; Sanz, E. *J. Chem. Phys.* **2006**, *125*, 074510.
- (24) Conde, M. M.; Vega, C. *J. Chem. Phys.* **2010**, *133*, 064507.
- (25) Guo, G.-J.; Zhang, Y.-G.; Li, M.; Wu, C.-H. *J. Chem. Phys.* **2008**, *128*, 194504.
- (26) Mutafschiev, B. *The Atomistic Nature of Crystal Growth*; Springer: Berlin, 2001; Chapter 12.
- (27) Duan, Z.; Möller, N.; Greenberg, J.; Weare, J. H. *Geochim. Cosmochim. Acta* **1992**, *56*, 1451.
- (28) Boewer, L.; Nase, J.; Paulus, M.; Lehmkuhler, F.; Tiemeyer, S.; Holz, S.; Pontoni, D.; Tolan, M. *J. Phys. Chem. C* **2012**, *116*, 8548.
- (29) Koga, T.; Wong, J.; Endoh, M. K.; Mahajan, D.; Gutt, C.; Sattja, S. K. *Langmuir* **2010**, *26*, 4627.
- (30) Walsh, M. R.; Beckham, G. T.; Koh, C. A.; Sloan, E. D.; Wu, D. T.; Sum, A. K. *J. Phys. Chem. C* **2011**, *115*, 21241.
- (31) Bagherzadeh, S. A.; Englezos, P.; Alavi, S.; Ripmeester, J. A. *J. Phys. Chem. C* **2012**, *116*, 24907.
- (32) Lu, W.; Chou, I. M.; Burruss, R. C. *Geochim. Cosmochim. Acta* **2008**, *72*, 412.
- (33) Ziparo, C.; Giannasi, A.; Ulivi, L.; Zoppi, M. *Int. J. Hydrogen Energy* **2011**, *36*, 7951.